Earth and Planetary Science Letters 396 (2014) 56–65

Contents lists available at ScienceDirect

Earth and Planetary Science Letters

www.elsevier.com/locate/epsl

Constraining shallow slip and tsunami excitation in megathrust ruptures using seismic and ocean acoustic waves recorded on ocean-bottom sensor networks

Jeremy E. Kozdon [a,*], Eric M. Dunham [b,c]

[a] Department of Applied Mathematics, Naval Postgraduate School, Monterey, CA, USA
[b] Department of Geophysics, Stanford University, Stanford, CA, USA
[c] Institute for Computational and Mathematical Engineering, Stanford University, Stanford, CA, USA

ARTICLE INFO

Article history:
Received 23 December 2013
Received in revised form 27 March 2014
Accepted 1 April 2014
Available online 18 April 2014
Editor: P. Shearer

Keywords:
tsunami
subduction zone
megathrust
early warning

ABSTRACT

Great earthquakes along subduction-zone plate boundaries, like the 2011 magnitude 9.0 Tohoku-Oki, Japan, event, deform the seafloor to generate massive tsunamis. Tsunami wave heights near shore are greatest when excitation occurs far offshore near the trench, where water depths are greatest and fault slip is shallow. The Tohoku event, featuring over 30 m of slip near the trench, exemplifies this hazard. Unfortunately the rupture process that far offshore is poorly constrained with land-based geodetic and even most seafloor deformation measurements, and seismic inferences of shallow slip are often nonunique. Here we demonstrate, through dynamic rupture simulations of the Tohoku event, that long-period guided waves in the ocean (specifically, leaking oceanic P-wave modes known as PL waves) can resolve the shallow rupture process and tsunami excitation near the trench. With predicted pressure changes of ~0.1–1 MPa along most of the seafloor landward of the trench, and periods of several seconds, these PL waves should be observable with ocean-bottom pressure sensors and/or seismometers. With cabled sensor networks like those being deployed offshore Japan and in other subduction zones, these waves could be used to rapidly quantify shallow slip and near-trench seafloor uplift and improve local tsunami early warning systems.

Published by Elsevier B.V.

1. Introduction

In subduction zones like the Japan Trench, the site of the 2011 M_w 9.0 Tohoku-Oki earthquake, coastal communities only have tens of minutes following a megathrust earthquake before the leading tsunami waves reach shore. In contrast, seismic waves, propagating an order of magnitude faster than tsunamis, arrive within about a minute. This travel-time difference provides an opportunity for local tsunami early warning systems. For earthquakes smaller than about M_w 8, a point source characterization of the earthquake in terms of magnitude, focal mechanism, and depth using seismic waves suffices to reliably estimate tsunami excitation (Hirshorn and Weinstein, 2009). For great earthquakes ($M_w > 8$), the spatial distribution of slip across the fault and the finite rupture duration begin to influence tsunamigenesis. Real-time slip inversions, such as those based on high-rate geodetic data (Blewitt et al., 2009; Ohta et al., 2012), can help predict tsunami wave heights. However, resolving the near-trench region ~100–200 km offshore, where tsunami excitation was largest in the Tohoku event (Sato et al., 2011; Ito et al., 2011; Kido et al., 2011; Fujiwara et al., 2011; Maeda et al., 2011), is challenging or even impossible using only land-based data (Ohta et al., 2012).

The resolution limits of land-based data can be overcome, of course, by placing instruments offshore, and the current revolution in seafloor geodesy and seismology holds much promise. Perhaps most relevant to local tsunami early warning systems are cabled sensor networks (Monastersky, 2012; Uehira et al., 2012; Saito, 2013), consisting of ocean-bottom pressure sensors and/or seismometers. These networks are directly linked to shore via fiber optic cables, thereby enabling real-time access to the data stream. Pressure sensors provide a rather direct measurement of tsunami wave heights as the waves pass overhead through the linear relation between pressure and the height of the water column under effectively hydrostatic conditions. Retrospective tsunami forecasts utilizing such data for the Tohoku event suggest that reliable

* Corresponding author.
E-mail addresses: jekozdon@nps.edu (J.E. Kozdon), edunham@stanford.edu (E.M. Dunham).

http://dx.doi.org/10.1016/j.epsl.2014.04.001
0012-821X/Published by Elsevier B.V.

estimates of wave heights can be obtained in about 20 min (Tsushima et al., 2011).

The pressure changes carried by the tsunami itself are neither the largest-amplitude nor the first-arriving signals from megathrust events at seafloor locations. Rapid seafloor uplift also excites seismic waves and ocean sound waves that propagate an order of magnitude faster than tsunamis. These include T waves, which are high-frequency (>2 Hz) sound waves trapped within the low-velocity SOFAR channel in the ocean. Despite initial optimism regarding their potential use for tsunami warning (Ewing et al., 1950), T waves appear to be too sensitive to small-scale details of the source process to reliably estimate the overall, lower-frequency earthquake source properties controlling tsunami excitation (Okal et al., 2003).

In addition to purely acoustic modes in the ocean, like T waves, offshore earthquakes also generate various guided waves involving motions of both the ocean and underlying solid. These include oceanic Rayleigh waves (Biot, 1952; Yamashita and Sato, 1976; Eyov et al., 2013) and leaking P-wave modes (also known as oceanic PL waves) (Oliver and Major, 1960; Phinney, 1961; Haddon, 1987), which are the subject of this work. We demonstrate, through simulations of the Tohoku earthquake, that PL waves excited by megathrust events are remarkably sensitive to shallow slip and seafloor uplift near the trench. The waves propagate toward shore at about 6 km/s (about 30 times faster than tsunami waves) and carry oscillatory pressure changes, at periods of several seconds, between 0.1 and 1 MPa across most of the seafloor landward of the trench. Acoustic organ-pipe reverberations in the ocean above the trench are also quite sensitive to near-trench motions. These various waves could be recorded by the same pressure sensor networks deployed for monitoring tsunamis, provided that the sampling rate and dynamic range of the instruments permit recording such signals without aliasing or clipping. These data could potentially be used to more rapidly and accurately infer tsunami wave heights.

2. Dynamic rupture simulations

We identified the link between PL waves and tsunami excitation through dynamic rupture simulations of the Tohoku earthquake (Kozdon and Dunham, 2013). Dynamic rupture simulations simultaneously solve for the slip history and seismic and acoustic wavefields that are consistent with the fault friction law, initial stresses, and the momentum balance and material response of the solid Earth and overlying compressible ocean. Using a dynamic, rather than kinematic, rupture model is not essential to study PL-wave excitation and propagation from megathrust events, but does provide an additional level of self-consistency in the source process.

The full details of our rupture models are given in Appendix A, and briefly summarized here. Because the Tohoku rupture extended nearly 500 km along strike and only 200 km down-dip we neglect variations in the along-strike direction. This renders the model two-dimensional, and allows us to focus on the up- and down-dip rupture growth that dominated most of the rupture process, particularly in the first minute or so (Ide et al., 2011; Yue and Lay, 2011). The method and model parameters are largely the same as those in the simulations of Kozdon and Dunham (2013), but with improvements to the structural model that are described below. Also, in contrast to our previous study, all simulations now have an ocean layer. The solid Earth response is linear elastic and the ocean is treated as a linear acoustic medium. We neglect gravitational restoring forces in the momentum balance, except in setting the initial tractions on the fault surface as described subsequently. The geometry and off-fault material properties (Fig. 1a) are based on the structural model of Miura et al. (2005). In our original simulations (Kozdon and Dunham, 2013), we directly used the nonplanar seafloor bathymetry and material interfaces observed along a seismic line extending off the Miyagi coast (Miura et al., 2005). The present model has smoother interfaces and bathymetry. The new bathymetry averages over along-strike bathymetric variations to provide a more representative profile. This proves useful when estimating the contribution to tsunami excitation from horizontal displacement of a sloping seafloor (Tanioka and Satake, 1996). The material properties are piecewise constant (see layer names in Fig. 1a) with values given in Table 1. The property values within each layer are identical to those in Kozdon and Dunham (2013); only the geometry is slightly altered.

We use a rate-and-state friction law in which fault shear resistance evolves with slip toward a steady state strength that is either an increasing or decreasing function of fault slip velocity (e.g., Rice et al., 2001). These behaviors are known as velocity-strengthening and velocity-weakening, respectively; the latter is necessary for unstable slip and earthquake nucleation while the former is usually associated with aseismic sliding. The depth dependence of frictional properties determines where and how fault slip occurs. We initially developed these simulations to study how frictional properties along the shallowest portion of the plate interface influence the ability of ruptures to reach the trench, finding that surface-breaking rupture is possible even through >30-km-long velocity-strengthening segments (Kozdon and Dunham, 2013).

In this work, we focus on a set of four simulations. All simulations have velocity-weakening friction on the central, seismogenic part of the plate interface, and transition to velocity-strengthening below 46.5 km depth. The latter is well-constrained by comparison to static displacement data on land and on the seafloor (Kozdon and Dunham, 2013). The models have different frictional properties on the upper part of the fault extending 30 km landward from the trench. That distance corresponds approximately to the length of the frontal prism, or deformed zone, at the trench (Tsuru et al., 2002). We label the four simulations based on the value of the rate-and-state $b-a$ parameter on the shallow fault as follows: velocity-weakening ($b-a=0.004$), neutrally stable ($b-a=0$), velocity-strengthening ($b-a=-0.004$), and extreme velocity-strengthening ($b-a=-0.008$). The central seismogenic zone has $b-a=0.004$. For the purposes of this exposition, the reader may simply view these as alternative source models with different amounts of slip near the trench.

We set initial effective normal stress on the upper section of the fault as the difference between lithostatic total normal stress and hydrostatic pore pressure. Below a certain depth we assume that pore pressure begins to track the lithostatic gradient, thus saturating the initial effective normal stress on the fault at a constant value $\bar{\sigma}_{\max}$ below that depth. The maximum effective stress $\bar{\sigma}_{\max}$ is the sole tunable model parameter that we select, in each of our four models, to obtain a reasonable fit to the onshore and offshore displacements. The values of $\bar{\sigma}_{\max}$ for the four models, from velocity-weakening to extreme velocity-strengthening, are $\bar{\sigma}_{\max}=$ 25 MPa, 30 MPa, 40 MPa, and 45 MPa, respectively. The corresponding values of $(b-a)\bar{\sigma}_{\max}$ in the central seismogenic zone are 0.1, 0.12, 0.16, and 0.2 MPa, respectively.

The resulting slip profiles (Fig. 2a) are nearly identical between the four models at depth, but differ substantially over the final ~50 km near the trench. This reflects a trade-off between the average stress drop at depth, which increases with increasing $\bar{\sigma}_{\max}$, and the effective length of the seismogenic zone, which decreases as the upper part of the fault becomes more velocity-strengthening. Also shown in Fig. 2 are fits to an onshore high-rate GPS displacement time series and to static seafloor displacement measurements. With the exception of the seafloor measurements closest to the trench (Ito et al., 2011), which are subject to large

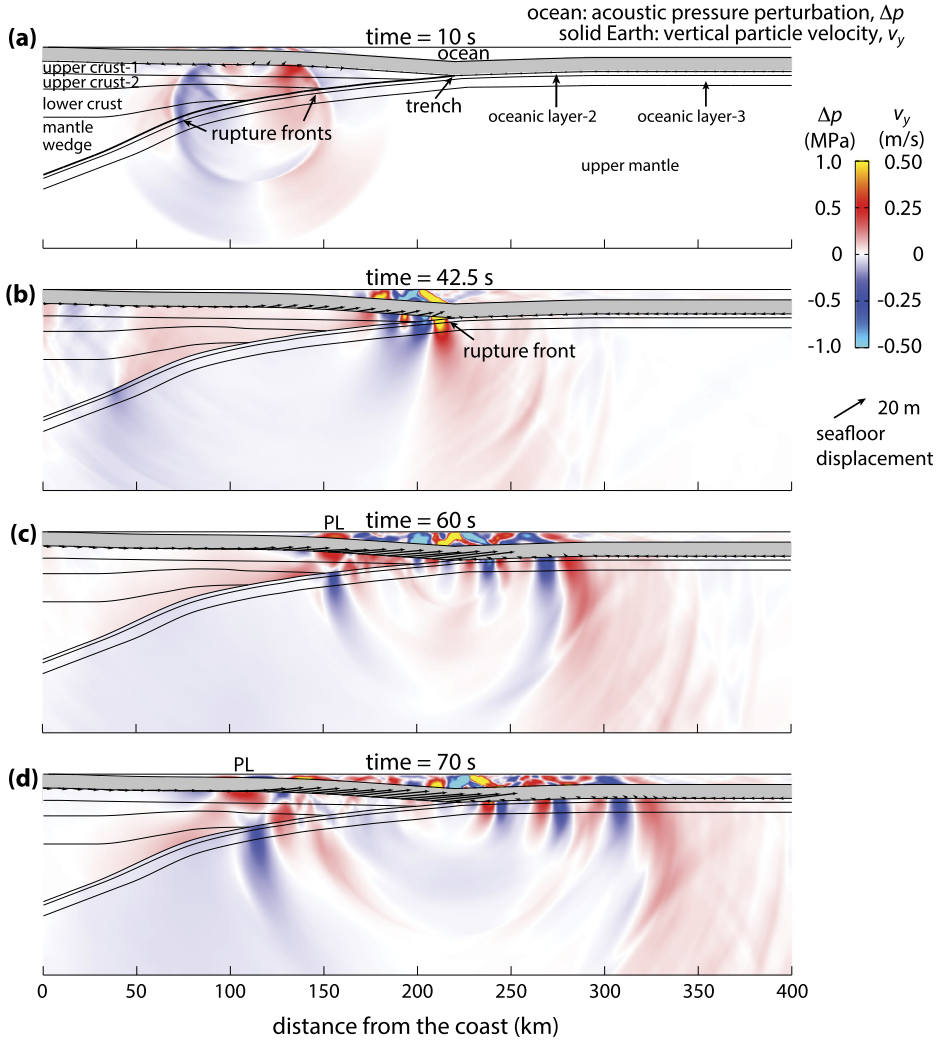

Fig. 1. Wavefield snapshots from a simulation with near-trench velocity-weakening friction. Colors show vertical particle velocity in the solid Earth and acoustic pressure perturbation in the ocean. The ocean is shifted upward to show seafloor displacement (arrows). (a) Bilateral rupture growth, with hypocentral P and S waves and early reflections visible. Structural units are labeled; material properties are given in Table 1. (b) Rupture reaches trench; note multiply reflected sound waves in ocean propagating at supersonic horizontal velocity. (c, d) Oceanic Rayleigh waves propagate offshore; PL waves propagate landward. (For interpretation of the references to color in this figure legend, the reader is referred to the web version of this article.)

Table 1
Material properties for structural model shown in Fig. 1a.

Layer name	P-wave speed (km/s)	S-wave speed (km/s)	Density (kg/m^3)
ocean	1.5	0	1000
upper crust-1	4.8	2.8	2200
upper crust-2	5.5	3.2	2600
lower crust	7.0	4.0	2800
mantle wedge	8.0	4.6	3200
oceanic layer-2	5.5	3.2	2600
oceanic layer-3	6.8	3.9	2800
uppermost mantle	8.0	4.6	3200

uncertainties, these data cannot be used to distinguish between the various models. The measurements close to the trench might also record landslides or slumping, as observed immediately landward of the trench in differential bathymetry (Fujiwara et al., 2011) and seismic reflection (Kodaira et al., 2012) studies.

These differences in shallow slip influence tsunami excitation, as illustrated in Fig. 2e through the predicted sea surface uplift immediately following the earthquake. Our simulations currently neglect gravitational restoring forces and thus these predictions are simply estimates employing several assumptions (instantaneous uplift of an incompressible, hydrostatic ocean, due to both vertical seafloor uplift and horizontal advection of bathymetric slopes (Tanioka and Satake, 1996)). It is essential, for local tsunami early warning systems, to be able to rapidly distinguish between these different models. As discussed in the Introduction, this can be most reliably accomplished by directly measuring the effectively hydrostatic pressure changes on the seafloor beneath the tsunami itself (Tsushima et al., 2011). But tsunamis propagate relatively slowly; their speed in the long-wavelength, or shallow-water, limit is $\sqrt{gH} \approx 200$ m/s, for gravitational acceleration g and ocean depth $H \approx 4$ km. Thus with this approach only instruments within a few tens of kilometers from the trench could be used to distinguish between these different models in the first few minutes after the earthquake. Pressure sensors close to shore would not detect tsunami waves from the near-trench region until nearly ten minutes later. In the following section, we discuss the potential use of PL waves to quantify near-trench tsunami excitation.

3. Seismic and ocean acoustic waves

The progression of the rupture and evolution of the seismic and acoustic wavefields from one of our simulations are shown in Fig. 1 and Videos 1 and 2. Space–time plots of slip velocity on the fault

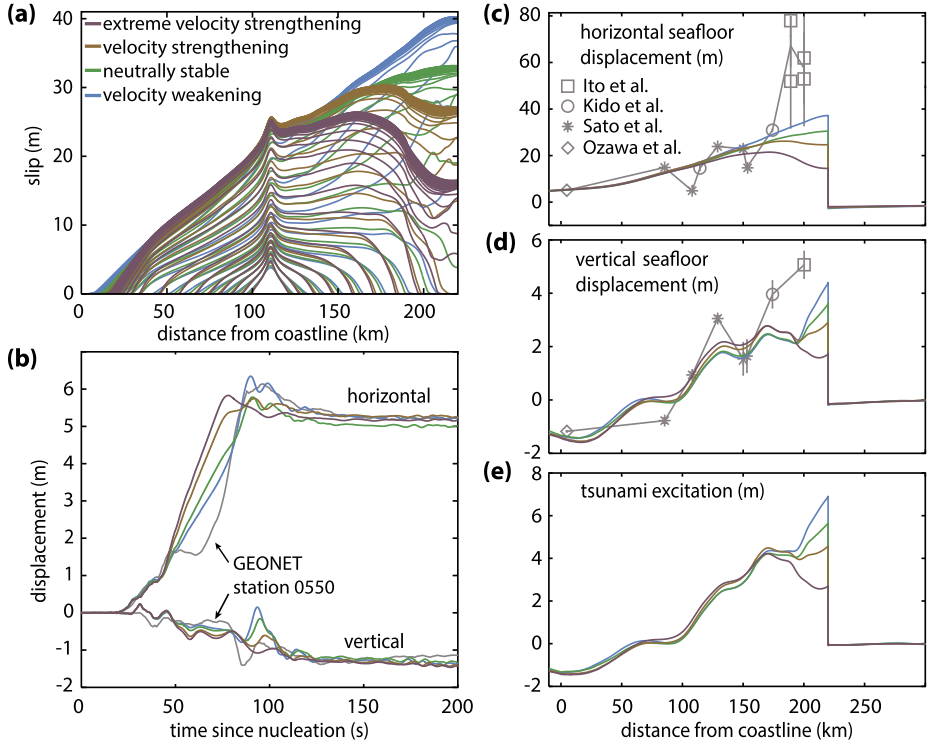

Fig. 2. (a) Slip histories (every 5 s) from simulations employing a range of possible frictional properties near the trench. Also shown are comparisons of model predictions with (b) 1-Hz GPS displacements recorded at the coast (GEONET station 0550 operated by the Geospatial Information Authority of Japan) and (c, d) static seafloor deformation measurements (Sato et al., 2011; Ito et al., 2011; Kido et al., 2011; Ozawa et al., 2011). (e) Predicted tsunami excitation, shown as initial sea surface elevation assuming instantaneous response of an incompressible, hydrostatic ocean. The models differ substantially near the trench, but this region cannot be resolved with land-based geodetic data.

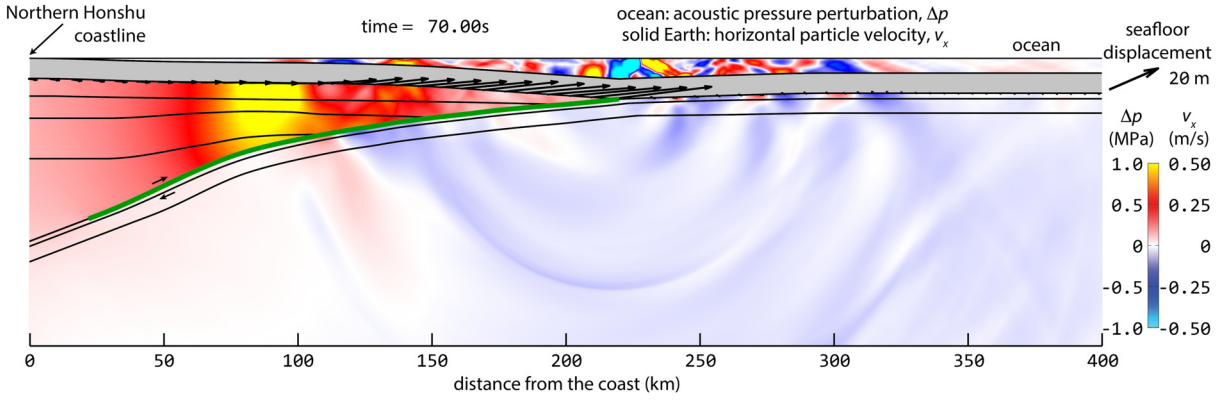

Video 1. Seismic and acoustic wavefield from 2011 Tohoku-Oki dynamic rupture simulation (velocity-weakening near trench). First few frames show P-wave velocity model and material structure. Later frames show evolution of horizontal particle velocity in the solid Earth and acoustic pressure perturbation in the ocean. The ocean is shifted upward to show seafloor displacement (arrows). The expanding green line marks the ruptured portion of the fault. (For interpretation of the references to color in this figure legend, the reader is referred to the web version of this article.)

are shown in Fig. 3a and b. After nucleating about 100 km offshore in the central velocity-weakening section of the fault, the rupture grows bilaterally. Down-dip propagation ceases before reaching the coastline as the fault becomes velocity-strengthening at depth. The rupture continues up-dip, eventually reaching the trench. Reflected waves drive a smaller, secondary rupture back down the fault, as suggested by some kinematic slip inversions (e.g., Ide et al., 2011). Rupture velocity along the shallow section of the fault is around 2.5–3 km/s in all models (Fig. 3a and b). The differences in near-trench friction across the models lead primarily to changes in the amount of shallow slip, and therefore potency rate in the near-trench region (Fig. 3c and d), rather than to any major transitions in rupture style. The rupture velocity is close to the S-wave speed of the surrounding material; we do not see the extremely fast, supershear speeds that Ma (2012) finds in his megathrust simulations with elastic off-fault response. Neither are there anomalously slow rupture and slip velocities like in tsunami earthquakes (Kanamori, 1972; Lay et al., 2012).

A large burst of seismic and acoustic waves are generated during rupture breakout. To better understand the wavefield, we present space–time plots of pressure changes and vertical velocity on the seafloor from our four models (Figs. 4 and 5). The various waves are labeled in Fig. 4a.

The abrupt artificial nucleation process we employ excites seismic waves that convert to acoustic waves within the ocean. Due to the large impedance contrast between the fluid and solid, the ocean sound waves retain rather large amplitudes over multiple reflections as the waves spread laterally away from the epicenter. We do not expect these waves (labeled “reverberations from artificial nucleation” in Fig. 4a) to have such large amplitudes in actual

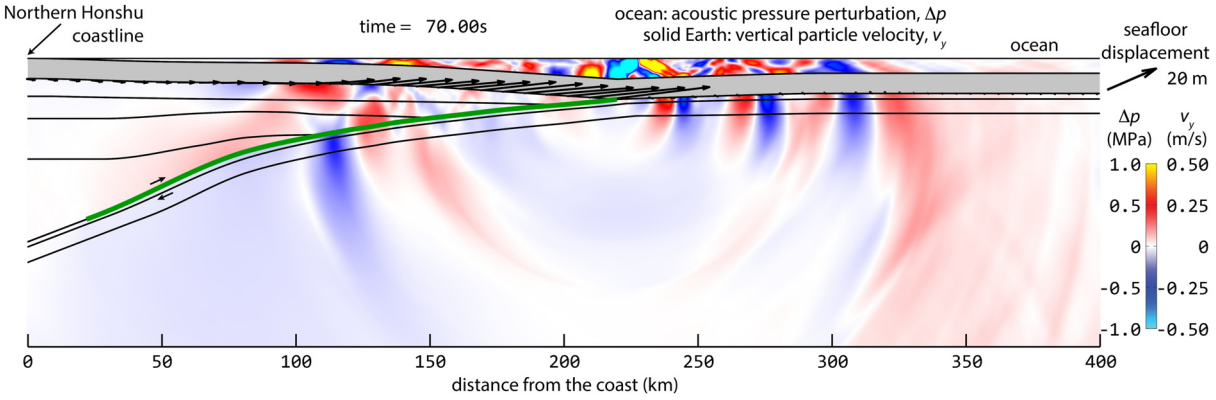

Video 2. Seismic and acoustic wavefield from 2011 Tohoku-Oki dynamic rupture simulation (velocity-weakening near trench). First few frames show P-wave velocity model and material structure. Later frames show evolution of vertical particle velocity in the solid Earth and acoustic pressure perturbation in the ocean. The ocean is shifted upward to show seafloor displacement (arrows). The expanding green line marks the ruptured portion of the fault. (For interpretation of the references to color in this figure legend, the reader is referred to the web version of this article.)

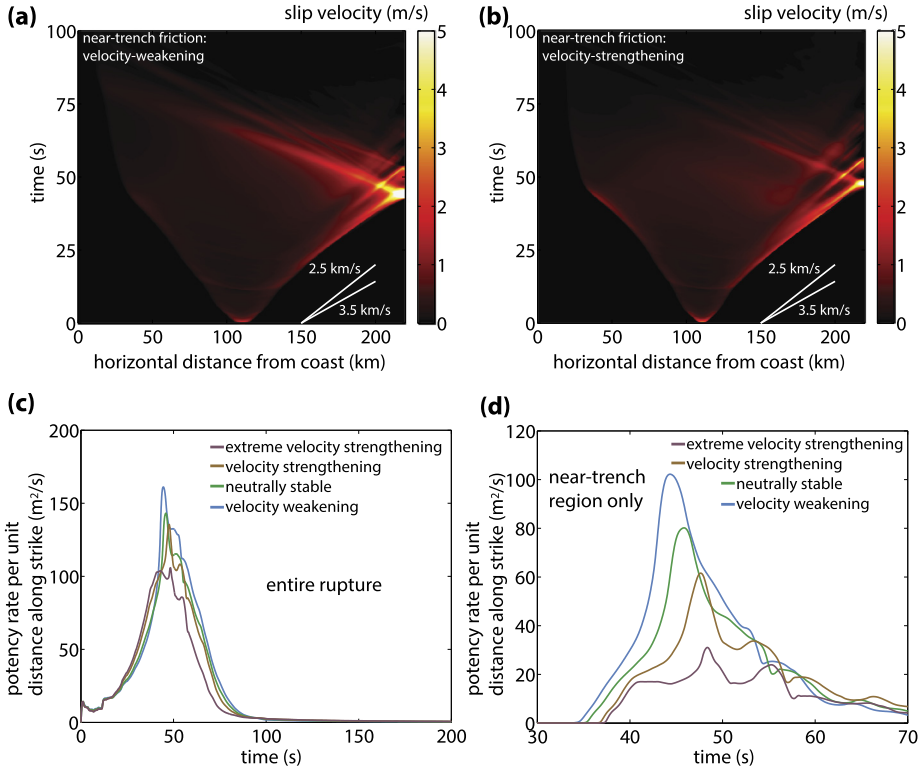

Fig. 3. Space–time plots of fault slip velocity for (a) near-trench velocity-weakening and (b) velocity-strengthening friction. Potency rate for (c) overall rupture process and (d) near-trench region (extending 30-km landward from trench).

earthquakes due to the much more gradual, and less coherent, nucleation process in nature.

As the rupture propagates up-dip, it excites sound waves in the ocean. At the rupture front is a region of intense fault-normal motion; given the nearly horizontal inclination of the fault, this manifests as an upward particle velocity (bright yellow velocities in Fig. 1b near arrow marking rupture front). This upward motion compresses the ocean above, exciting an ocean acoustic wave with positive pressure perturbation (bright yellow pressures in Fig. 1b directly above rupture front). These waves undergo multiple reflections between the sea surface and seafloor, and have planar wavefronts (essentially Mach fronts) because the rupture is propagating faster than the ocean sound speed. The first reflection off of the sea surface changes the sign of the pressure perturbation, and when this wave reaches the seafloor it pulls it upward (evident in the other yellow velocity pulse in Fig. 1b around 190 km from the coast). This unclamps the fault and creates a secondary peak in slip velocity that is evident in Fig. 3a and b.

Rapid uplift of the seafloor around the trench excites an acoustic organ-pipe mode with ≈14-s period above the trench (labeled "organ pipe" in Fig. 4a). This mode is comprised of vertically propagating sound waves that bounce between the seafloor and sea surface with characteristic period $4H/c_f \approx 14$ s, where H is the ocean depth and c_f is the fluid sound speed (Miyoshi, 1954). This mode has vertical wavelength of $\approx 4H$ and a temporal quality factor exceeding ten due to the high impedance contrast between the ocean and solid Earth (Haddon, 1987). The amplitude of the organ-pipe waves correlates well with seafloor uplift. These waves have been observed during the 2003 M_w 8.3 Tokachi-Oki, Japan, earthquake using pressure sensors offshore Hokkaido (Nosov and Kolesov, 2007; Chierici et al., 2010).

The largest signals following rupture breakout are large-amplitude surface waves channeled offshore within the ocean and

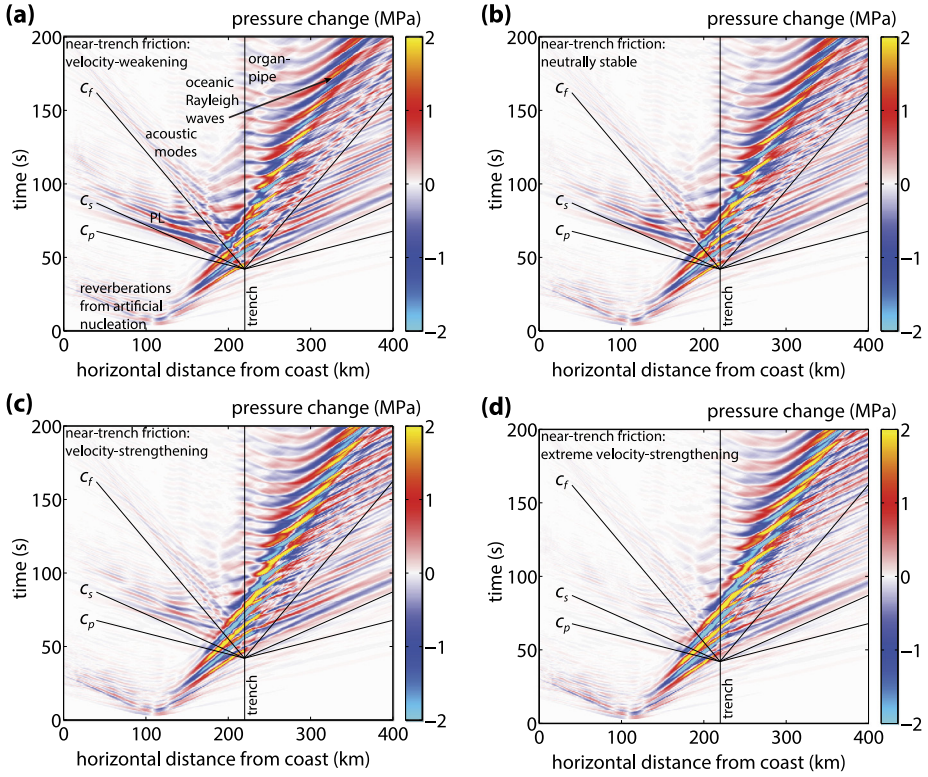

Fig. 4. Space–time plots of pressure change on the seafloor. Lines show wave speeds: $c_f = 1.5$ km/s (ocean sound speed), $c_p = 7$ km/s and $c_s = 4$ km/s (lower crust P- and S-wave speeds). PL waves traveling from the trench toward shore at 6 km/s and organ-pipe reverberations above the trench have amplitudes that correlate with shallow slip and near-trench seafloor uplift. Large-amplitude oceanic Rayleigh waves propagate offshore at group velocities slightly less than the ocean sound speed. Shown for models with different near-trench frictional properties: (a) velocity-weakening, (b) neutrally stable, (c) velocity-strengthening, (d) extreme velocity-strengthening.

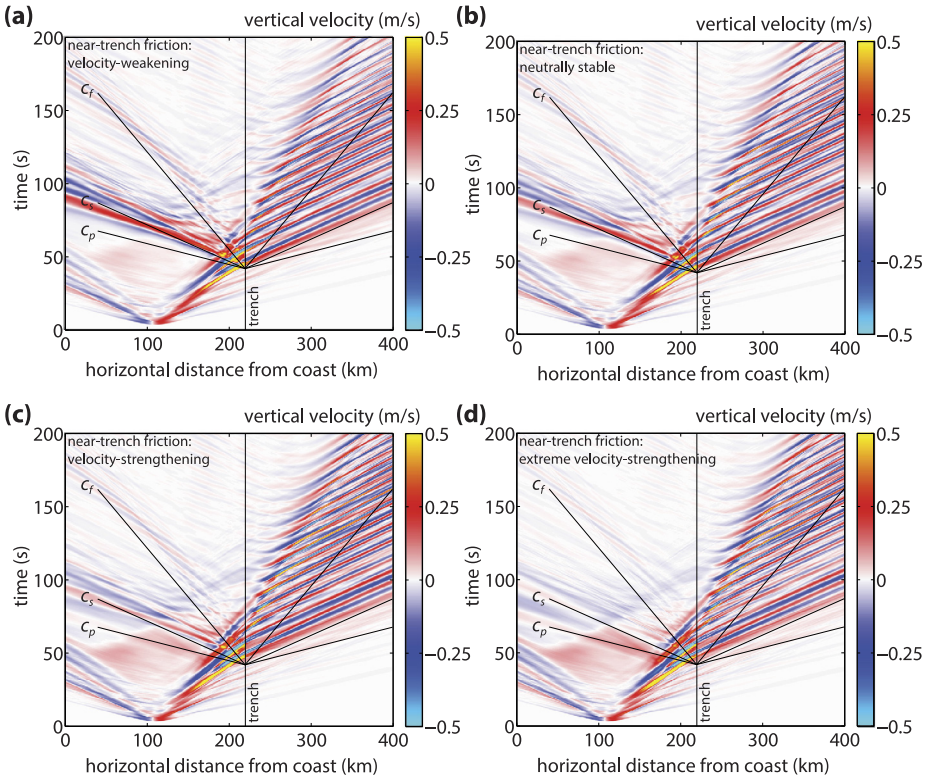

Fig. 5. Same as Fig. 4, but for vertical particle velocity on the seafloor.

underlying oceanic crust. Amplitudes, which exceed 1 MPa in terms of acoustic pressure changes in the ocean, are enhanced by forward directivity due to the largely up-dip propagation. The dominant period of these waves is again ≈14 s, like the organ-pipe mode, and there is likely some connection between the pronounced excitation at this period and the resonance of ocean acoustic waves undergoing multiple reflections off of the seafloor and sea surface.

We identify these surface waves as fundamental mode oceanic Rayleigh waves. Insight can be gained by examining dispersion curves for Rayleigh waves in a structural model consisting of a uniform depth ocean over an elastic half-space (Biot, 1952). At long periods (compared to the time it takes a sound wave to propagate over the ocean depth), the influence of the ocean layer is negligible and these are effectively Rayleigh waves in an elastic half-space. At very short periods, these waves become Stoneley waves (also known as Scholte waves) that are confined to the fluid–solid interface, and have phase velocities slower than both the fluid sound speed and the solid S-wave speed. The ≈14-s waves seen in our simulations fall in between these two limits, and in that intermediate period range, the phase velocity is between the ocean sound speed and the solid Rayleigh-wave speed, and the group velocity is somewhat less than the ocean sound speed. These features are clearly seen in Fig. 4a, where these waves are labeled “oceanic Rayleigh waves”. See also Videos 1 and 2, where individual phases can be seen emerging on the landward side of the wave packet and advancing offshore faster than the overall seaward propagation of the wave packet.

There have been several observations of oceanic Rayleigh waves with these characteristics. Nakanishi (1992) noted a large-amplitude wave packet, appearing well after P- and S-wave arrivals, in seismograms recorded on Hokkaido from several shallow earthquakes offshore the Kuril Islands. This phase had a characteristic ≈15-s period and an arrival time corresponding to a group velocity less than the ocean sound speed. The deep water along the trench acts as a waveguide for surface waves at these periods (Nakanishi, 1992; Yomogida et al., 2002). While such an effect cannot be studied in our two-dimensional simulations, it is possible that the oceanic Rayleigh waves generated by subduction events could be studied using seafloor instruments deployed along the trench. These waves can then couple back into standard Rayleigh waves, with much faster group velocities, when entering shallow water near land (Noguchi et al., 2013).

We next turn our attention to waves that propagate from the trench back toward the coast, as these are the most useful ones for constraining the near-trench rupture process and for providing tsunami early warning. The largest-amplitude and fastest-propagating waves are PL waves that travel landward at 6 km/s and have characteristic 4-s period (labeled “PL” in Fig. 1c, d and Fig. 4a). The 4-s period might be related to the duration of the potency rate pulse associated with shallow slip (Fig. 3d).

We identify these waves as leaking P-wave modes in the oceanic waveguide (Oliver and Major, 1960; Phinney, 1961; Haddon, 1987) for several reasons. They propagate faster than the fastest S-wave speed in our model, which immediately rules out all surface waves. They have an oscillatory character indicative of multiple reflections within a low-velocity waveguide (the ocean and upper crust), but propagate at a speed close to the P-wave speed of deeper, fast layers. As evident in Fig. 1c, d and Videos 1 and 2, these waves have large amplitudes in both the ocean (where they take the form of sound waves) and the solid Earth. Oceanic PL waves are multiply reflected sound waves partially trapped in the ocean but penetrating into the underlying solid Earth as evanescent P waves and radiating S waves (Oliver and Major, 1960; Phinney, 1961; Haddon, 1987). PL waves have phase velocities exceeding the S-wave speed of the underlying solid, and attenuate

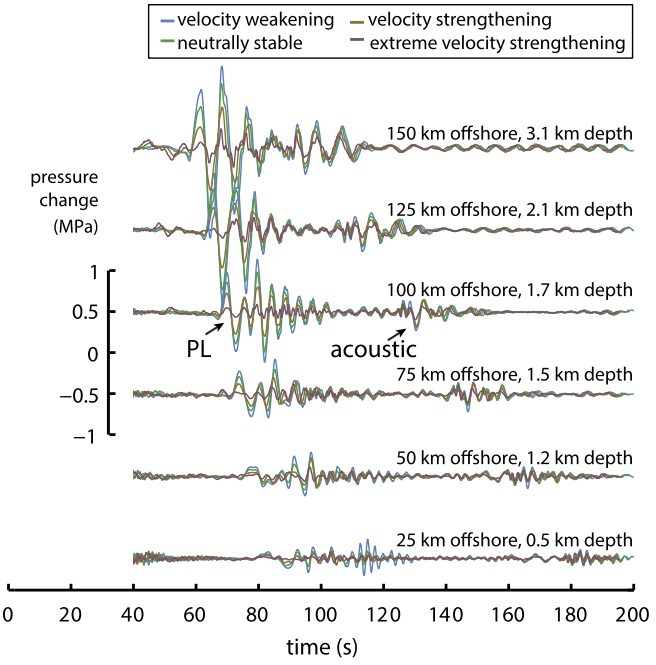

Fig. 6. Acoustic pressure perturbations on the seafloor, landward of the trench. Unrealistic reverberations from the artificial nucleation process, which appear in the first tens of seconds, are not shown.

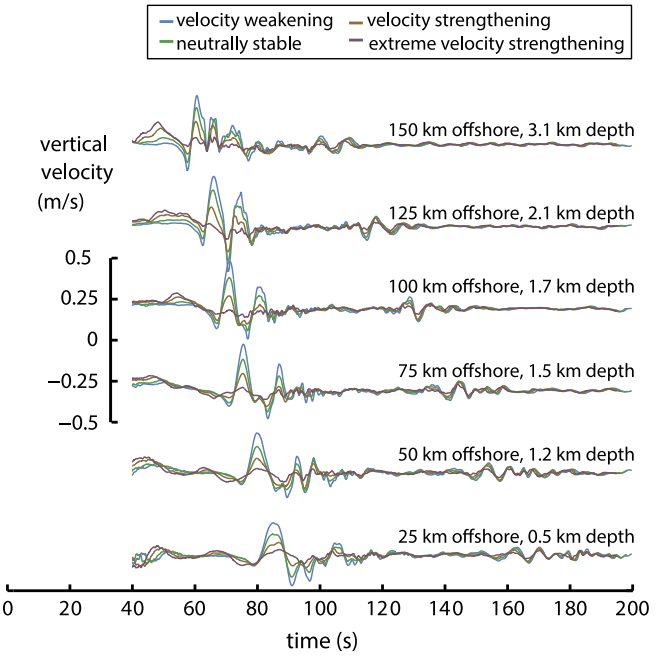

Fig. 7. Vertical particle velocities on the seafloor, landward of the trench. Unrealistic reverberations from the artificial nucleation process, which appear in the first tens of seconds, are not shown.

as they propagate due to S-wave radiation (hence the terminology leaking mode). The waves in our simulations also feature prograde particle motion on the seafloor, another distinctive characteristic of PL waves (Phinney, 1961). While oceanic PL waves carry large acoustic pressure changes in the ocean, they are quite distinct from purely acoustic T-wave modes, which are higher frequency (>2 Hz) sound waves trapped within the low-velocity SOFAR channel (Okal et al., 2003).

In our simulations, PL waves have amplitudes of ∼0.1–1 MPa over most of the seafloor landward of the trench. They are not

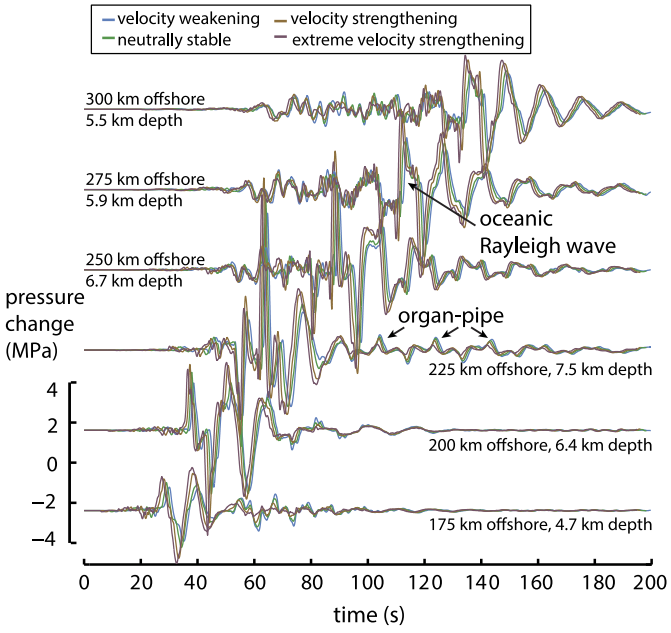

Fig. 8. Acoustic pressure perturbations on the seafloor, farther offshore.

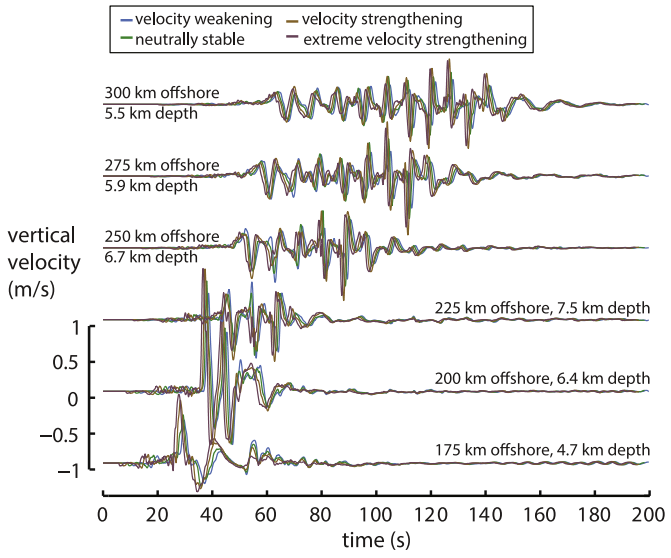

Fig. 9. Vertical particle velocities on the seafloor, farther offshore.

only expressed as pressure perturbations in the ocean (Fig. 4), but also in the solid-Earth particle velocity on the seafloor, particularly the vertical component (Fig. 5), with amplitudes around ∼0.1–0.5 m/s. With an eye toward detection of these waves using ocean-bottom sensor networks, we present pressure and velocity seismograms at several seafloor locations, both landward of the trench (Figs. 6 and 7) and farther offshore (Figs. 8 and 9).

PL waves can be identified out to distances of about 175 km from the coast, beyond which interference with other waves excited near the trench by the propagating rupture overly complicates the waveforms. The waves become less visible, at least in terms of seafloor pressure changes, when the water depth becomes too shallow. Similarly, using three-dimensional simulations of waves generated by the Tohoku earthquake, Maeda et al. (2013) found significant trapping of P waves within the ocean, thereby reducing P-wave amplitudes on land compared to simulations lacking an ocean layer. Waves in the solid Earth do continue propagating onto land, and the differences between the models that are evident in the seafloor vertical particle velocity persist there as well.

What is most remarkable is the strong correlation between PL-wave amplitudes and near-trench seafloor uplift (Fig. 1c). This indicates a high degree of sensitivity of these waves to the near-trench source process, and a lack of sensitivity to the deeper rupture process. This is confirmed in Fig. 3d, which shows the potency rates from the shallow part of the fault. These qualities can potentially be exploited to augment estimates of seafloor uplift (and tsunami excitation) using land-based data, which has a complementary sensitivity to the source process.

Later arrivals labeled as “acoustic modes” in Fig. 4 have shorter periods and travel closer to the sound speed in the ocean. These are probably a combination of fundamental- and higher-mode surface waves, which have phase and group velocities close to the sound speed at short periods (Biot, 1952; Yamashita and Sato, 1976; Eyov et al., 2013). These waves have received some attention in the literature, with some authors suggesting their potential use for tsunami warning systems (Stiassnie, 2010; Eyov et al., 2013). However, accurate prediction of waveforms arriving around this time likely requires accounting for the low-velocity SOFAR channel, especially at frequencies >2 Hz to properly capture T waves (which are not modeled in our simulations). We therefore caution that this part of our synthetic seismograms might be overly simple and somewhat unrealistic.

In contrast to the high sensitivity of PL waves to the shallow rupture process, the oceanic Rayleigh waves that propagate offshore (Figs. 8 and 9) have essentially identical amplitudes for all models. Their amplitudes instead seem to be determined by the overall moment release along the entire seismogenic zone. While they would therefore be of no use in illuminating the near-trench rupture process specifically, these waves could be used for magnitude estimates.

4. Discussion

Our simulations suggest that PL waves can be used to distinguish between the different rupture models presented in this work. Observation of large-amplitude PL waves implies coseismic occurrence of shallow slip. However, we caution that the absence of notable PL waves from megathrust events does not rule out the excitation of a large tsunami. This is because PL waves, which have ≈4-s period in our simulations, are probably sensitive to the time scale over which near-trench seafloor uplift occurs. In our simulations, this happens rapidly (over ∼10 s) as part of the normal coseismic rupture process, rather than over the minute or greater time scales that likely characterize tsunami earthquakes (Kanamori, 1972; Okal et al., 2003). While this sensitivity is not desirable for tsunami warning, distinguishing between anomalously slow slip or typically fast slip would provide much-needed insight into tsunamigenesis by shallow fault slip near the toe of subduction zones. PL waves might also help distinguish if tsunami excitation occurs by near-trench landslides or by pervasive inelastic deformation of sediments in the frontal prism (Ma, 2012), rather than elastic seafloor displacement by coseismic slip.

While our results appear quite promising, it is well worth emphasizing the fundamental difficulty of using relatively high-frequency waves (like PL waves) to infer tsunami excitation, which depends solely on much longer period seafloor motions. Additional complexities that we have not included in our model might influence the period and amplitude of PL waves. For example, the frontal prisms in the Japan Trench and other subduction zones contain extremely compliant, low-velocity sediments. Seismic studies of the Japan Trench (Tsuru et al., 2002; Miura et al., 2005; Kodaira et al., 2012) show P-wave velocities in the range of 1–3 km/s within the frontal prism, which extends landward

for about 10–30 km from the trench. Similarly, Poisson's ratio in this region is likely higher than the nominal value of 0.25 that we have assumed here. It is possible that the rupture would decelerate in this region, relative to what is seen in our simulations, and that seafloor uplift might increase (Tanioka and Seno, 2001). These changes in the near-trench rupture process might alter the correlation between PL-wave amplitude and tsunami excitation. There is a clear need for additional simulations to examine these processes in greater detail.

Looking forward, it is desirable to validate our model predictions against actual data. PL waves from the Tohoku event were likely recorded at two ocean-bottom pressure sensors, TM1 and TM2, off the Sanriku coast (Maeda et al., 2011; Tsushima et al., 2011), but to the best of our knowledge the unfiltered waveforms have not been published. At a water depth of 1.63 km (corresponding to TM1), our models predict peak-to-peak pressure changes carried by PL waves of 1.05 MPa (velocity-weakening), 0.85 MPa (neutrally stable), 0.58 MPa (velocity-strengthening), and 0.19 MPa (extreme velocity-strengthening). Our simulations also predict a 4-s period for these waves. We do not presently understand what sets this characteristic period, but speculate based on the near-trench potency rate history (Fig. 3d) that it might be related to the spatial extent of rapid, near-trench seafloor uplift, or the time scale over which that uplift occurs.

In addition to being observable on seafloor pressure sensors, PL waves could also be detected with ocean-bottom seismometers. Because large pressure changes are carried throughout the water column, due to the long wavelengths of PL waves, they might even be observable with SOFAR-channel hydrophones, like those in the International Monitoring System (Yildiz et al., 2013). However, such instruments are typically designed to detect vastly smaller signals; it is likely that broadband seismometers, hydrophones, and differential pressure gauges would clip on the large-amplitude waves generated by megathrust events. Absolute pressure gauges and strong motion accelerometers would probably be needed, and even those would require sufficiently high sampling rates. Finally, because PL waves cause changes in sea surface height exceeding 1 m, one might consider detection systems employing surface buoys. However, ∼1-m oscillations at periods of a few seconds might not be easily distinguishable from the usual ocean swell without observation of extremely fast move-out (compared to surface gravity waves) across arrays of surface buoys.

Our simulations suggest how local tsunami early warning systems utilizing offshore instruments might be improved by incorporating additional data associated with acoustic and seismic waves. Sensor networks with absolute pressure gauges and ocean bottom seismometers, like those being deployed along the Japan Trench (Monastersky, 2012; Uehira et al., 2012; Saito, 2013), appear most promising. These would likely benefit from closer station spacings or array configurations that would avoid spatial aliasing of these ∼20-km-wavelength PL waves.

Acknowledgements

This work was supported by the National Science Foundation (OCI-1122734 to J.E.K., EAR-1255439 to E.M.D.) and the Alfred P. Sloan Foundation (BR2012-097 to E.M.D.). We thank Shin'ichi Miyazaki for providing the GEONET data, and the two anonymous reviewers for insightful comments.

Appendix A. Numerical simulation details

The fault obeys the rate-and-state friction law (Rice et al., 2001; Kozdon and Dunham, 2013)

$$\frac{d\tau}{dt} = \frac{a\bar{\sigma}}{V}\tanh\left(\frac{\tau}{a\bar{\sigma}}\right)\frac{dV}{dt} - \frac{V}{L}\left[|\tau| - \bar{\sigma} f_{ss}(V)\right], \tag{A.1}$$

with steady state friction coefficient

$$f_{ss}(V) = f_0 - (b-a)\ln(V/V_0), \tag{A.2}$$

in which τ is the shear strength of the fault, V is the slip velocity, $\bar{\sigma}$ is the effective normal stress, a and b are dimensionless rate-and-state friction parameters, L is the state evolution distance, and f_0 is the friction coefficient for steady sliding at reference velocity V_0. The sign of $b-a$ determines if steady state frictional strength decreases ($b-a>0$, velocity-weakening) or increases ($b-a<0$, velocity-strengthening) with increasing slip velocity. With this form of the friction law, shear strength does not respond instantaneously to abrupt changes in effective normal stress. This is particularly important to avoid ill-posedness (Rice et al., 2001) that can arise in bimaterial sliding problems for friction laws in which τ is directly proportional to the instantaneous value of $\bar{\sigma}$.

Some frictional properties are spatially uniform ($f_0 = 0.6$, $V_0 = 1$ μm/s, and $L = 0.8$ m), while others (a and b) vary with depth. Over most of the fault, $a = 0.016$ and $b = 0.02$ such that $b-a = 0.004$ and fault slip is unstable. To control the down-dip extent of rupture, we increase a such that $b-a$ becomes negative (velocity-strengthening) below 46.5 km depth. That depth is chosen to match vertical seafloor displacement and onshore displacement data (Kozdon and Dunham, 2013).

We present four models that have differing frictional properties, and hence rupture behavior, in the near-trench region. Specifically, we vary b (while retaining $a = 0.016$) along the upper part of the fault, extending 30 km horizontally from the trench, with values given in the main text. These four models also differ in terms of initial stress conditions as described below, but are otherwise identical.

We account for undrained poroelastic alterations of fault-zone pore pressure, Δp, in response to changes in total normal stress, $\Delta\sigma$, using a linear relation of the form $\Delta p = B\Delta\sigma$, where $B = 0.6$. Thus,

$$\bar{\sigma} = \bar{\sigma}_0 + (1-B)\Delta\sigma, \tag{A.3}$$

where $\bar{\sigma}_0$ is the initial effective normal stress on the fault prior to the rupture. Poroelastic effects thus partially buffer slip-induced changes in normal stress that occur on dipping faults and on faults juxtaposing dissimilar elastic solids; both effects occur in our simulations. This simple poroelastic model emerges as a limiting case of a more rigorous model (Cocco and Rice, 2002) when the fault is bordered by highly damaged material; in that case, B is Skempton's coefficient.

We set initial effective normal stress $\bar{\sigma}_0$ as described in the main text. The initial shear stress on the fault is set to $0.6\bar{\sigma}_0$. With the specific form of the rate-and-state law we use, we must also set the initial slip velocity V_{ini}. This is equivalent to setting the initial state variable in standard forms of rate-and-state friction; both approximately determine the peak strength of the fault. We use $V_{ini} = 1$ μm/s. Ruptures are nucleated by rapidly increasing shear stress over a small section of the fault at the desired hypocentral location, following the procedure in Kozdon and Dunham (2013).

The combined system of equations is solved using the numerical method developed by Kozdon et al. (2013). The wave equations governing the elastic solid and acoustic fluid layers are solved using a multiblock finite difference method. The domain is divided into 42 four-sided blocks, potentially with curvilinear boundaries, separated by 71 interfaces. All material interfaces, and the fault, coincide with one or more of these computational interfaces. Normal and shear tractions are balanced across solid–solid interfaces, while only normal tractions are balanced across fluid–solid interfaces (at which shear tractions vanish). Each block is mapped to a rectangle in the computational domain and high-order summation-by-parts finite-difference operators are used to

discretize the equations in the transformed coordinate system. The fundamental unknown fields in the medium are the stress changes and particle velocities, which are defined at all grid points and time steps (in contrast to staggered-grid finite-difference methods). An acoustic medium is obtained as a limiting case of an elastic medium by taking shear modulus (and hence shear-wave speed) to zero. Interface conditions, including the nonlinear fault friction law, are enforced weakly using penalty terms added to the semi-discrete system of equations. The overall method is provably stable and accurate.

Appendix B. Supplementary material

Supplementary material related to this article can be found online at http://dx.doi.org/10.1016/j.epsl.2014.04.001.

References

Biot, M.A., 1952. The interaction of Rayleigh and Stoneley waves in the ocean bottom. Bull. Seismol. Soc. Am. 42, 81–93.

Blewitt, G., Hammond, W.C., Kreemer, C., Plag, H.-P., Stein, S., Okal, E., 2009. GPS for real-time earthquake source determination and tsunami warning systems. J. Geod. 83, 335–343. http://dx.doi.org/10.1007/s00190-008-0262-5.

Chierici, F., Pignagnoli, L., Embriaco, D., 2010. Modeling of the hydroacoustic signal and tsunami wave generated by seafloor motion including a porous seabed. J. Geophys. Res. 115. http://dx.doi.org/10.1029/2009JC005522.

Cocco, M., Rice, J.R., 2002. Pore pressure and poroelasticity effects in Coulomb stress analysis of earthquake interactions. J. Geophys. Res. 107. http://dx.doi.org/10.1029/2000JB000138.

Ewing, M., Tolstoy, I., Press, F., 1950. Proposed use of the T phase in tsunami warning systems. Bull. Seismol. Soc. Am. 40, 53–58.

Eyov, E., Klar, A., Kadri, U., Stiassnie, M., 2013. Progressive waves in a compressible-ocean with an elastic bottom. Wave Motion 50, 929–939. http://dx.doi.org/10.1016/j.wavemoti.2013.03.003.

Fujiwara, T., Kodaira, S., No, T., Kaiho, Y., Takahashi, N., Kaneda, Y., 2011. The 2011 Tohoku-Oki earthquake: displacement reaching the trench axis. Science 334, 1240. http://dx.doi.org/10.1126/science.1211554.

Haddon, R.A.W., 1987. Response of an oceanic wave guide to an explosive point source using leaking modes. Bull. Seismol. Soc. Am. 77, 1804–1822.

Hirshorn, B., Weinstein, S., 2009. Earthquake source parameters, rapid estimates for tsunami warning. In: Meyers, R.A. (Ed.), Encyclopedia of Complexity and Systems Science. Springer-Verlag, pp. 2657–2675.

Ide, S., Baltay, A., Beroza, G.C., 2011. Shallow dynamic overshoot and energetic deep rupture in the 2011 Mw 9.0 Tohoku-Oki earthquake. Science 332, 1426–1429. http://dx.doi.org/10.1126/science.1207020.

Ito, Y., Tsuji, T., Osada, Y., Kido, M., Inazu, D., Hayashi, Y., Tsushima, H., Hino, R., Fujimoto, H., 2011. Frontal wedge deformation near the source region of the 2011 Tohoku-Oki earthquake. Geophys. Res. Lett. 38. http://dx.doi.org/10.1029/2011GL048355.

Kanamori, H., 1972. Mechanism of tsunami earthquakes. Phys. Earth Planet. Inter. 6, 346–359.

Kido, M., Osada, Y., Fujimoto, H., Hino, R., Ito, Y., 2011. Trench-normal variation in observed seafloor displacements associated with the 2011 Tohoku-Oki earthquake. Geophys. Res. Lett. 38. http://dx.doi.org/10.1029/2011GL050057.

Kodaira, S., No, T., Nakamura, Y., Fujiwara, T., Kaiho, Y., Miura, S., Takahashi, N., Kaneda, Y., Taira, A., 2012. Coseismic fault rupture at the trench axis during the 2011 Tohoku-oki earthquake. Nat. Geosci. 5, 646–650. http://dx.doi.org/10.1038/ngeo1547.

Kozdon, J.E., Dunham, E.M., 2013. Rupture to the trench: dynamic rupture simulations of the 11 March 2011 Tohoku earthquake. Bull. Seismol. Soc. Am. 103, 1275–1289. http://dx.doi.org/10.1785/0120120136.

Kozdon, J.E., Dunham, E.M., Nordström, J., 2013. Simulation of dynamic earthquake ruptures in complex geometries using high-order finite difference methods. J. Sci. Comput. 55, 92–124. http://dx.doi.org/10.1007/s10915-012-9624-5.

Lay, T., Kanamori, H., Ammon, C.J., Koper, K.D., Hutko, A.R., Ye, L., Yue, H., Rushing, T.M., 2012. Depth-varying rupture properties of subduction zone megathrust faults. J. Geophys. Res. 117. http://dx.doi.org/10.1029/2011JB009133.

Ma, S., 2012. A self-consistent mechanism for slow dynamic deformation and tsunami generation for earthquakes in the shallow subduction zone. Geophys. Res. Lett. 39. http://dx.doi.org/10.1029/2012GL051854.

Maeda, T., Furumura, T., Noguchi, S., Takemura, S., Sakai, S., Shinohara, M., Iwai, K., Lee, S.J., 2013. Seismic and tsunami wave propagation of the 2011 off the Pacific Coast of Tohoku earthquake as inferred from the tsunami-coupled finite difference simulation. Bull. Seismol. Soc. Am. 103, 1456–1472. http://dx.doi.org/10.1785/0120120118.

Maeda, T., Furumura, T., Sakai, S., Shinohara, M., 2011. Significant tsunami observed at ocean-bottom pressure gauges during the 2011 off the Pacific coast of Tohoku earthquake. Earth Planets Space 63, 803–808. http://dx.doi.org/10.5047/eps.2011.06.005.

Miura, S., Takahashi, N., Nakanishi, A., Tsuru, T., Kodaira, S., Kaneda, Y., 2005. Structural characteristics off Miyagi forearc region, the Japan Trench seismogenic zone, deduced from a wide-angle reflection and refraction study. Earth Planet. Sci. Lett. 407, 165–188. http://dx.doi.org/10.1016/j.tecto.2005.08.001.

Miyoshi, H., 1954. Generation of the tsunami in compressible water (part I). J. Oceanogr. Soc. Jpn. 10, 1–9.

Monastersky, R., 2012. Tsunami forecasting: the next wave. Nature 483, 144–146. http://dx.doi.org/10.1038/483144a.

Nakanishi, I., 1992. Rayleigh waves guided by sea-trench topography. Geophys. Res. Lett. 19, 2385–2388. http://dx.doi.org/10.1029/92GL02438.

Noguchi, S., Maeda, T., Furumura, T., 2013. FDM simulation of an anomalous later phase from the Japan Trench subduction zone earthquakes. Pure Appl. Geophys. 170, 95–108. http://dx.doi.org/10.1007/s00024-011-0412-1.

Nosov, M.A., Kolesov, S.V., 2007. Elastic oscillations of water column in the 2003 Tokachi-Oki tsunami source: in-situ measurements and 3-D numerical modelling. Nat. Hazards Earth Syst. Sci. 7, 243–249.

Ohta, Y., Kobayashi, T., Tsushim, H., Miura, S., Hino, R., Takasu, T., Fujimoto, H., Iinuma, T., Tachibana, K., Demachi, T., Sato, T., Ohzono, M., Umino, N., 2012. Quasi real-time fault model estimation for near-field tsunami forecasting based on RTK-GPS analysis: application to the 2011 Tohoku-Oki earthquake (Mw 9.0). J. Geophys. Res. 117. http://dx.doi.org/10.1029/2011JB008750.

Okal, E.A., Alasset, P.-J., Hyvernaud, O., Schindelé, F., 2003. The deficient T waves of tsunami earthquakes. Geophys. J. Int. 152, 416–432. http://dx.doi.org/10.1046/j.1365-246X.2003.01853.x.

Oliver, J., Major, M., 1960. Leaking modes and the PL phase. Bull. Seismol. Soc. Am. 50, 165–180.

Ozawa, S., Nishimura, T., Suito, H., Kobayashi, T., Tobita, M., Imakiire, T., 2011. Coseismic and postseismic slip of the 2011 magnitude-9 Tohoku-Oki earthquake. Nature 475, 373–376. http://dx.doi.org/10.1038/nature10227.

Phinney, R.A., 1961. Leaking modes in the crustal waveguide: 1. The oceanic PL wave. J. Geophys. Res. 66, 1445–1469. http://dx.doi.org/10.1029/JZ066i005p01445.

Rice, J.R., Lapusta, N., Ranjith, K., 2001. Rate and state dependent friction and the stability of sliding between elastically deformable solids. J. Mech. Phys. Solids 49, 1865–1898. http://dx.doi.org/10.1016/S0022-5096(01)00042-4.

Saito, T., 2013. Dynamic tsunami generation due to sea-bottom deformation: analytical representation based on linear potential theory. Earth Planets Space 65, 1411–1423. http://dx.doi.org/10.5047/eps.2013.07.004.

Sato, M., Ishikawa, T., Ujihara, N., Yoshida, S., Fujita, M., Mochizuki, M., Asada, A., 2011. Displacement above the hypocenter of the 2011 Tohoku-Oki earthquake. Science 332, 1395. http://dx.doi.org/10.1126/science.1207401.

Stiassnie, M., 2010. Tsunamis and acoustic-gravity waves from underwater earthquakes. J. Eng. Math. 67, 23–32. http://dx.doi.org/10.1007/s10665-009-9323-x.

Tanioka, Y., Satake, K., 1996. Tsunami generation by horizontal displacement of ocean bottom. Geophys. Res. Lett. 23, 861–864. http://dx.doi.org/10.1029/96GL00736.

Tanioka, Y., Seno, T., 2001. Sediment effect on tsunami generation of the 1896 Sanriku Tsunami earthquake. Geophys. Res. Lett. 28, 3389–3392. http://dx.doi.org/10.1029/2001GL013149.

Tsuru, T., Park, J.-O., Miura, S., Kodaira, S., Kido, Y., Hayashi, T., 2002. Along-arc structural variation of the plate boundary at the Japan Trench margin: implication of interplate coupling. J. Geophys. Res. 107. http://dx.doi.org/10.1029/2001JB001664.

Tsushima, H., Hirata, K., Hayashi, Y., Tanioka, Y., Kimura, K., Sakai, S., Shinohara, M., Kanazawa, T., Hino, R., Maeda, K., 2011. Near-field tsunami forecasting using offshore tsunami data from the 2011 off the Pacific coast of Tohoku earthquake. Earth Planets Space 63, 821–826. http://dx.doi.org/10.5047/eps.2011.06.052.

Uehira, K., Kanazawa, T., Noguchi, S., Aoi, S., Kunugi, T., Matsumoto, T., Okada, Y., Sekiguchi, S., Shiomi, K., Shinohara, M., Yamada, T., 2012. Ocean bottom seismic and tsunami network along the Japan Trench. Abstract OS41C-1736 presented at 2012 Fall Meeting. AGU, San Francisco, CA, 3–7 Dec.

Yamashita, T., Sato, R., 1976. Correlation of tsunami and sub-oceanic Rayleigh wave amplitudes: possibility of the use of Rayleigh wave in tsunami warning system. J. Phys. Earth 24, 397–416.

Yildiz, S., Sabra, K., Dorman, L.M., Kuperman, W.A., 2013. Using hydroacoustic stations as water column seismometers. Geophys. Res. Lett. 40, 2573–2578. http://dx.doi.org/10.1002/grl.50371.

Yomogida, K., Okuyama, R., Nakanishi, I., 2002. Anomalous Rayleigh-wave propagation along oceanic trench. Stud. Geophys. Geod. 46, 691–710. http://dx.doi.org/10.1023/A:1021129405870.

Yue, H., Lay, T., 2011. Inversion of high-rate (1 sps) GPS data for rupture process of the 11 March 2011 Tohoku earthquake (Mw 9.1). Geophys. Res. Lett. 38. http://dx.doi.org/10.1029/2011GL048700.